DRAFT VERSION NOVEMBER 26, 2018
Preprint typeset using LaTeX style emulateapj v. 12/16/11

DETAILED ELEMENTAL ABUNDANCES IN THE M31 STELLAR HALO: LOW-RESOLUTION RESOLVED STELLAR SPECTROSCOPY

IVANNA ESCALA
Department of Astronomy, California Institute of Technology, 1200 E California Blvd, Pasadena, CA, 91125, USA

EVAN N. KIRBY
Department of Astronomy, California Institute of Technology, 1200 E California Blvd, Pasadena, CA, 91125, USA

KAROLINE M. GILBERT
Space Telescope Science Institute, 3700 San Martin Drive, Baltimore, MD 21218, USA and
Department of Physics & Astronomy, Bloomberg Center for Physics and Astronomy, John Hopkins University, 3400 N. Charles St, Baltimore, MD 21218, USA

EMILY C. CUNNINGHAM
Department of Astronomy and Astrophysics, University of California, Santa Cruz, 1156 High St, Santa Cruz, CA, 95064, USA

JENNIFER WOJNO
Department of Physics & Astronomy, Bloomberg Center for Physics and Astronomy, John Hopkins University, 3400 N. Charles St, Baltimore, MD 21218, USA

Draft version November 26, 2018

ABSTRACT

Measurements of [Fe/H] and [α/Fe] can probe the minor merging history of a galaxy, providing a direct way to test the hierarchical assembly paradigm. While measurements of [α/Fe] have been made in the stellar halo of the Milky Way, little is known about detailed chemical abundances in the stellar halo of M31. To make progress with existing telescopes, we apply spectral synthesis to low-resolution DEIMOS spectroscopy (R $\sim$ 2500 at 7000 Å) across a wide spectral range (4500 Å $< \lambda <$ 9100 Å). By applying our technique to low-resolution spectra of 135 red giant branch (RGB) stars in 4 MW globular clusters, we demonstrate that our technique reproduces previous measurements from higher resolution spectroscopy. Based on the intrinsic dispersion in [Fe/H] and [α/Fe] of individual stars in our combined cluster sample, we estimate systematic uncertainties of $\sim$0.11 dex and $\sim$0.04 dex in [Fe/H] and [α/Fe], respectively. We apply our method to deep, low-resolution spectra of 14 RGB stars in the smooth halo of M31, resulting in higher signal-to-noise per spectral resolution element compared to DEIMOS medium-resolution spectroscopy, given the same exposure time and conditions. We find $\langle$[α/Fe]$\rangle$ = 0.49 $\pm$ 0.31 dex and $\langle$[Fe/H]$\rangle$ = $-$1.53 $\pm$ 0.52 dex for our sample. This implies that the smooth halo field is likely composed of disrupted dwarf galaxies with truncated star formation histories that were accreted early in the formation history of M31.

Subject headings: stars: abundances – galaxies: abundances – galaxies: halos – galaxies: formation – Local Group

1. INTRODUCTION

Stellar chemical abundances are a key component in determining the origins of stellar halos of Milky Way (MW) like galaxies, providing insight into the formation of galaxy-scale structure. The long dynamical times of stellar halos allow tidal features to remain identifiable in phase space, in terms of kinematics and chemical abundances, for Gyr timescales. Stellar chemical abundances of stars retain information about star formation history and accretion times of progenitor satellite galaxies, even when substructures can no longer be detected by kinematics alone. In particular, measurements of metallicity[1] and α-element abundances provide a way of directly testing the hierarchical assembly paradigm central to ΛCDM cosmology, providing a fossil record of the formation environment of stars accreted onto the halo.

The [α/Fe] ratio serves as a useful diagnostic of formation history, given that it traces the star formation timescales of a galaxy (e.g., Gilmore & Wyse 1998). Type II supernovae (SNe) produce abundant α-elements (O, Ne, Mg, Si, S, Ar, Ca, and Ti), increasing [α/Fe], whereas Type Ia SNe produce Fe-rich ejecta, reducing [α/Fe]. While measurements of [α/Fe] have been made in the stellar halo of the MW, little is known about the detailed chemical abundances of the stellar halo of M31. A comparable understanding of the properties of the MW and M31 stellar halos is required to verify basic assumptions about how the MW evolved, where such assumptions are used to extrapolate MW-based results to studies of galaxies beyond the Local Group.

Although high-resolution ($R \gtrsim$ 15,000), high signal-to-noise (S/N) spectra enables simultaneous measurements of a star's temperature, surface gravity, and individual element abundances based on individual lines, it is impractical to

E-mail: ie@astro.caltech.edu

[1] We define metallicity in terms of stellar iron abundance, [Fe/H], where [Fe/H] = $\log_{10}(n_{\rm Fe}/n_{\rm H}) - \log_{10}(n_{\rm Fe}/n_{\rm H})_{\odot}$

achieve high enough S/N for traditional high-resolution spectroscopic abundance analysis (e.g., Kirby & Cohen 2012) for red giant branch (RGB) stars at the distance of M31 (783 kpc; Stanek & Garnavich 1998).

It is possible to obtain spectroscopic metallicity measurements of M31 RGB stars from medium-resolution spectra ($R \sim 6000$) using spectral synthesis (e.g., Kirby et al. 2008a). This method leverages the entire spectrum's metallicity information simultaneously, enabling measurements of abundances from relatively low S/N spectra. Kirby et al. (2008b, 2010, 2013) successfully measured [Fe/H] and [α/Fe] in MW globular clusters (GCs), MW dwarf spheroidal (dSph) satellite galaxies, and Local Group dwarf irregular galaxies, showing that abundances can be measured to a precision of ~ 0.2 dex from spectra with S/N ~ 15 Å^{-1}.

Only in 2014 has spectral synthesis been applied to individual RGB stars in the M31 system for the first time (Vargas et al. 2014a,b). Existing spectroscopic chemical abundance measurements in M31 are primarily based on metallicity estimates from the strength of the calcium triplet (Chapman et al. 2006; Koch et al. 2008; Kalirai et al. 2009; Richardson et al. 2009; Tanaka et al. 2010; Ibata et al. 2014; Gilbert et al. 2014; Ho et al. 2015). Vargas et al. (2014a) measured [α/Fe] and [Fe/H] for a total of 226 red giants in 9 M31 satellite galaxies. Although Vargas et al. (2014a) measured [α/Fe] for 9 M31 dSphs, only a single dSph, And V, shows a clear chemical abundance pattern, where [α/Fe] declines with [Fe/H]. However, the present spectroscopic sample size and measurement uncertainties of the And V data enable only qualitative conclusions about the chemical evolution of the dSph. Obtaining more quantitative descriptions of the chemical enrichment and star formation histories of the M31 system requires higher S/N spectroscopic data, which results in smaller uncertainties on abundance measurements. Only then can one-zone numerical chemical evolution models (Lanfranchi & Matteucci 2003, 2007, 2010; Lanfranchi et al. 2006; Kirby et al. 2011b) be reliably applied to measurements to derive star formation and mass assembly histories.

Although Vargas et al. (2014a,b) demonstrated the feasibility of measuring [Fe/H] and [α/Fe] at the distance of M31, measuring [Fe/H] and [α/Fe] more precisely requires deep ($\sim$6 hour) observations with DEIMOS using the 600 line mm^{-1} grating to yield higher S/N for the same exposure time and observing conditions. For magnitudes fainter than $I_0 \sim 21$ (0.5 magnitudes below the tip of M31's RGB), sky line subtraction at $\lambda > 7000$ Å becomes the dominant source of noise in DEIMOS spectra observed with the 1200 line mm^{-1} grating. Given the access to blue optical wavelengths granted by the 600 line mm^{-1} grating, its spectra are less susceptible to the effects of sky noise. Additionally, using the 600 line mm^{-1} grating achieves higher S/N per pixel for stars as faint as $I_0 \sim 21.8$.

Although using the 600 line mm^{-1} grating with DEIMOS results in a gain in S/N and wavelength coverage, it corresponds to a decrease in spectral resolution ($\sim$2.8 Å FWHM, or R ~ 2500 at 7000 Å, compared to $\sim$1.3 Å and R ~ 5400 for 1200 line mm^{-1}). Increasing the spectral range compensates for the decrease in spectral resolution, given the increase in the amount of available abundance information contained in the spectrum resulting from the higher density of absorption features at bluer optical wavelengths.

In this paper, we expand upon the technique first presented by Kirby et al. (2008a), applying spectral synthesis to low-resolution spectroscopy (LRS; R ~ 2500) across a wide spectral range ($\lambda \sim 4500$ - 9100 Å). In § 2, we describe our data reduction and GC observations. § 3 and § 4 detail our preparations to the observed spectrum and the subsequent abundance analysis. This includes a presentation of our new line list and grid of synthetic spectra. In § 5, we illustrate the efficacy of our technique applied to MW GCs and compare our results to chemical abundances from high-resolution spectroscopy in § 6. We quantify the associated systematic uncertainties in § 7. We conclude by measuring [α/Fe] and [Fe/H] in a M31 stellar halo field in § 8 and summarize in § 9.

TABLE 1
MW Globular Cluster Observations

Object	Date	θ_s[a] (")	X[b]	$t_{\rm exp}$[c] (s)	N[d]
NGC 2419	2015 Oct 9	0.6	1.23	2×1380	52
NGC 1904 (M79)	2015 Oct 8	0.8	1.40	2×1260	16
NGC 6864 (M75)	2015 May 19	0.9	1.56	3×1080	34
NGC 6341 (M92)	2018 Oct 11	0.6	1.52	6×300	33

[a]Seeing in arcseconds
[b]Air mass
[c]Total exposure time
[d]Number of RGB members per slitmask.

2. OBSERVATIONS

We utilize observations of Galactic GCs (Table 1) taken using KeckII/DEIMOS (Faber et al. 2003) to validate our LRS method of spectral synthesis. For our science configuration (both for MW GCs and M31 observations, § 8.1), we used the GG455 filter with a central wavelength of 7200 Å, in combination with the 600ZD grating and 0.7" slitwidths. The spectral resolution is approximately ~ 2.8 Å FWHM, compared to ~ 1.3 Å FWHM for the 1200 line mm^{-1} grating used in prior observations (Kirby et al. 2010, 2013). The wavelength range for each spectrum obtained with the 600ZD grating is within 4100 Å – 1 μm, where we generally omit $\lambda \lesssim 4500$ Å, owing to poor S/N in this regime and the presence of the G band. We also omit $\lambda > 9100$ Å, which extends beyond the wavelength coverage of our grid of synthetic spectra (§ 4.2).

To extract one-dimensional spectra from the raw DEIMOS data, we used a modification of version 1.1.4 of the data reduction pipeline developed by the DEEP2 Galaxy Redshift Survey (Cooper et al. 2012; Newman et al. 2013). Guhathakurta et al. (2006) provides a detailed description of the data reduction process. Modifications to the software include those of Simon & Geha (2007), where the pipeline was re-purposed for bright unresolved stellar sources (as opposed to faint, resolved galaxies). In addition, we include custom modifications to correct for atmospheric refraction in the two-dimensional raw spectra, which affects bluer optical wavelengths, and to identify lines in separate arc lamp spectra, as opposed to a single stacked arc lamp spectrum.

3. PREPARING THE SPECTRUM FOR ABUNDANCE MEASUREMENT

3.1. *Telluric Absorption Correction*

Unlike the red side of the optical (6300 - 9100 Å), there is no strong telluric absorption in the bluer regions (4500 - 6300 Å). As such, we do not make any corrections to the observed stellar spectra to take into account absorption from Earth's atmosphere in this wavelength range.

For the red (6100 - 9100 Å), we correct for the absorption

of Earth's atmosphere using the procedure described in Kirby et al. (2008a). We adopt HD066665 (B1V), observed on April 23, 2012 with an airmass of 1.081, using a long slit in the same science configuration (§ 2) as our data, as our spectrophotometric standard.

3.2. *Spectral Resolution Determination*

In contrast to Kirby et al. (2008a), who determined the spectral resolution as a function of wavelength based on the Gaussian widths of hundreds of sky lines, we assume a constant resolution, expressed as the typical FWHM of an absorption line, across the entire observed spectrum ($\sim$4500–9100 Å). Owing to the dearth of sky lines at bluer wavelengths, the number of available sky lines is insufficient to reliably determine the resolution as a function of wavelength. As an alternative, we introduce an additional parameter, $\Delta\lambda$, or the spectral resolution, into our chi-squared minimization, which determines the best-fit synthetic spectrum for each observed spectrum (§ 4.5).

3.3. *Continuum Normalization*

It is necessary to normalize the observed flux by its slowly varying stellar continuum in order to meaningfully compare to synthetic spectra for the abundance determination (§ 4.5). To obtain reliable abundances from spectral synthesis of low- and medium-resolution spectra dominated by weak absorption features, the continuum determination must be accurate (Shetrone et al. 2009; Kirby et al. 2009). This is particularly important for bluer wavelengths, where absorption lines are so numerous and dense that we cannot define "continuum regions" (Kirby et al. 2008a) in the blue. Instead, we utilize the entire observed spectrum, excluding regions with strong telluric absorption and bad pixels, to determine the continuum for 4500 – 9100 Å. In contrast to Kirby et al. (2008a), we do not utilize continuum regions at redder wavelengths (6300 - 9100 Å), despite the fact that they can be reliably defined, to maintain consistency in the continuum normalization method between each wavelength region of the observed spectrum.

We determined the initial continuum fit to the raw observed spectrum, which we shift into the rest frame, using a third-order B-spline with a breakpoint spacing of 200 pixels, excluding 5 pixels around the chip gap and at the start and stop wavelengths of the observed spectrum. In all steps, we weighted the spline fit by the inverse variance of each pixel in the observed spectrum. We performed sigma clipping, such that pixels that deviate by more than 5σ (0.1σ) above (below) the fit are excluded from the subsequent continuum determination, where σ is the inverse square root of the inverse variance array. We did not perform the fit iteratively beyond the above steps, given that our stringent criterion to prevent the numerous absorption lines from offsetting our continuum determination can eliminate a significant fraction of the pixels from subsequent iterations of the fit.

To further refine our continuum determination, we recalculate the continuum fit iteratively in the initial step of the abundance analysis (§ 4.5). Once we have found a best-fit synthetic spectrum, we divide the continuum-normalized observed spectrum by the best-fit synthetic spectrum to construct a "flat noise" spectrum, which captures the higher order terms in the observed spectrum not represented in the fit. We fit a third-order B-spline with a breakpoint spacing of 100 pixels to the flat noise spectrum, excluding 3σ deviant (above and below the fit) pixels, dividing the continuum-normalized observed spectrum by this fit. The modified continuum-normalized spectrum is then used in the next iteration of the continuum refinement until convergence is achieved (§ 4.5).

TABLE 2
SPECTRAL FEATURES (4100 - 6300 Å)

Feature	Wavelength(s) (Å)
Hδ	4101.734
Ca I	4226.730
G band (CH absorption)	4300-4315
Hγ	4340.462 (4335-4345)[a]
Hβ	4861.35 (4856-4866)
Mg I (b4)	5167.322
Mg I (b2)	5172.684
Mg I (b1)	5183.604
Mg H	4845,5622
Na D1,D2	5895.924,5889.951 (5885-5905)

[a]Wavelength regions indicated in paranthesis indicate regions that are omitted from the spectral fit.

3.4. *Custom Pixel Masks*

In addition to wavelength masks corresponding to a particular abundance (§ 4.4), we constructed a pixel mask for each analyzed observed spectrum. Typically excluded regions include 5 pixels on either side of the chip gap between the blue and red sides of the CCD, areas with improper sky line subtraction, the region around the Na D1 and D2 lines (5585 - 5905 Å), and other apparent instrumental artifacts. Table 2 includes a summary of prominent spectral features in DEIMOS spectra between 4100 - 6300 Å, where wavelength ranges given in parenthesis indicate regions that are masked. For example, we excluded 10 Å regions around Hγ (4335 - 4345 Å) and Hβ (4856 - 4866 Å). MOOG does not incorporate the effects of non-local thermodynamic equilibrium and thus cannot properly model the strong Balmer lines. If necessary, we also masked regions where the initial continuum fit failed, most often owing to degrading signal-to-noise as a function of wavelength at bluer wavelengths ($\lesssim$ 4500 Å). As for the red (6300 - 9100 Å), we adopted the pixel mask from Kirby et al. (2008a), which excludes spectral features such as the Ca II triplet, Hα, and regions with strong telluric absorption.

3.5. *Signal-to-Noise Estimation*

We estimate S/N per Angstrom for objects observed with the 600 line mm^{-1} grating from wavelength regions of the spectrum utilized in the initial continuum determination (§ 3.3). Given that we cannot define continuum regions for wavelengths blueward of 6300 Å, we calculate the S/N after the continuum refinement process (§ 4.5). We estimate the noise as the deviation between the continuum-refined observed spectrum and the best-fit synthetic spectrum and the signal as the best-fit synthetic spectrum itself. The S/N estimate per pixel is the mean of the S/N as a function of wavelength calculated from these quantities, where we exclude pixels that exceed the average noise threshold by more than 3σ. To convert to units of per Angstrom, we multiply this quantity by the inverse square root of the pixel scale ($\sim$ 0.64 Å for the 600 line mm^{-1} grating).

4. CHEMICAL ABUNDANCE ANALYSIS

Here, we present a new library of synthetic spectra in the range 4100 - 6300 Å. In this section, we describe our procedure for spectral synthesis in the blue, where we use our new

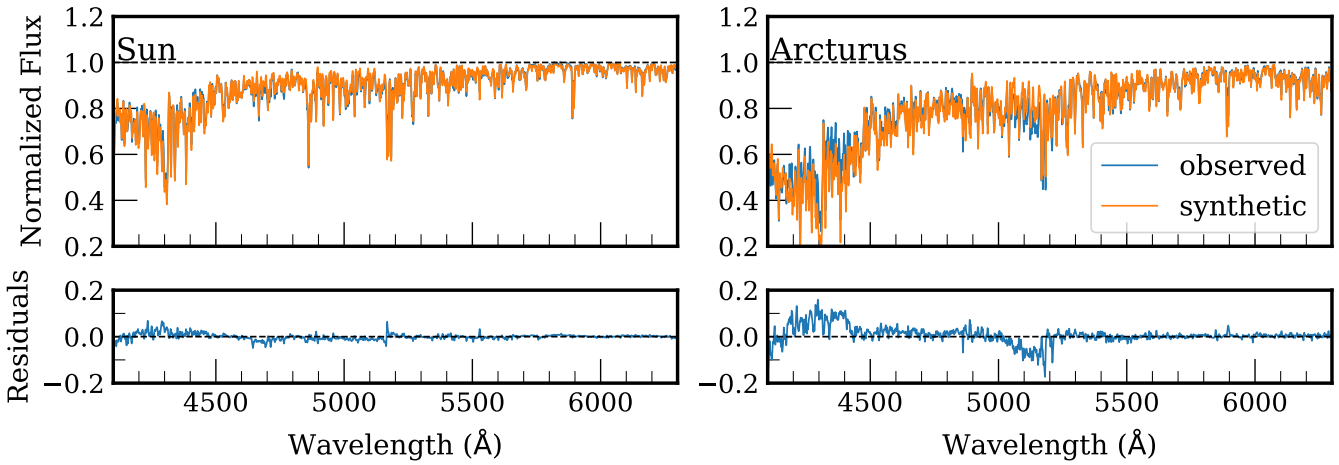

FIG. 1.— (*Top*) A comparison between high-resolution spectra (Hinkle et al. 2000) (*blue*) of the Sun (*left*) and Arcturus (*right*) and synthetic spectra (*orange*) generated using the blue line list (§ 4.1). Both spectra are smoothed to the expected resolution of the DEIMOS 600ZD grating (∼ 2.8 Å). For a description of synthetic spectrum generation, see § 4.2. (*Bottom*) The difference between the observed and synthetic spectra for the Sun and Arcturus. To improve the agreement between the synthetic and observed spectra, we have manually vetted the line list, adjusting the oscillator strengths of discrepant atomic transitions as necessary. In this process, we have favored the Sun over Arcturus, thus the larger residuals between the observed and synthetic spectra for the latter star (which has a lower effective temperature).

TABLE 3
BLUE LINE LIST (4100 - 6300 Å)

Wavelength (Å)	Species[a]	EP[b] (eV)	log gf[c]
5183.409	57.1	0.403	-0.6
5183.414	69.1	4.744	-2.65
5183.436	24.1	6.282	-3.172
5183.465	26.0	3.111	-5.06
5183.466	27.0	4.113	-1.187
5183.493	106.00112	3.244	-2.848
5183.506	106.00113	1.569	-3.974
5183.518	607.0	1.085	-4.211
5183.544	26.0	5.064	-3.886
5183.55	58.1	1.706	-2.27
5183.565	106.00112	3.55	-2.811
5183.578	607.0	1.204	-2.653
5183.598	23.1	6.901	-3.568
5183.604	12.0	2.717	-0.167
5183.615	607.0	1.085	-3.003
5183.683	607.0	1.205	-4.499
5183.683	106.00113	1.29	-4.921
5183.686	106.00113	2.371	-3.586
5183.708	40.0	0.633	-1.62
5183.709	22.1	1.892	-2.535
5183.748	58.1	1.482	-1.56
5183.794	106.00112	1.43	-2.866
5183.803	24.0	5.277	-3.52

Note. —The line list presented here is a subset of the entire line list, which spans 4100 - 6300 Å. The range of wavelengths presented here spans 0.4 Å around the strong Mg I line at 5183.604 Å. The line list is formatted to be compatible with MOOG.
[a] A unique code corresponding to chemical species. For example, 12.0 indicates Mg I, 22.1 indicates Ti II, 106.00112 indicates CN for carbon-12, and 106.0113 indicates CN for carbon-13.
[b] Excitation potential.
[c] Oscillator strength. Transitions modified in the vetting process have less than three decimal places.

grid in conjunction with the red grid of Kirby et al. (2008a) to measure abundances across an expanded optical range (4100 - 9100 Å).

4.1. *Line List*

We constructed a line list of wavelengths, excitation potentials (EPs), and oscillator strengths (log gf) for atomic and molecular transitions in the spectral range covering 4100 - 6300 Å for stars in our stellar parameter range ($T_{\rm eff} > 4000$ K). We queried the Vienna Atomic Line Database (VALD; Kupka et al. 1999) and the National Institute of Standards and Technology (NIST) Atomic Spectra Database (Kramida et al. 2016) for all transitions of neutral or singly ionized atoms with EP < 10 eV and log $gf > -5$, supplementing the line list with molecular (Kurucz 1992) and hyperfine transitions (Kurucz 1993). All Fe I line oscillator strengths from Fuhr & Wiese (2006) are included in the NIST database.

Next, we compared synthetic spectra (§ 4.2) of the Sun and Arcturus, generated from our line list and model stellar atmospheres, to high resolution spectra (Hinkle et al. 2000) of the respective stars. We adopted $T_{\rm eff}$ = 5780 K, log g = 4.44 dex, [Fe/H] = 0 dex, and [α/Fe] = 0 dex for the Sun. For Arcturus, we adopted $T_{\rm eff}$ = 4300 K, log g = 1.50 dex, and [Fe/H] = -0.50 dex, and [α/Fe] = 0 dex (Peterson et al. 1993).

To produce agreement between the synthetic and observed spectra, we vetted the line list by manually adjusting the oscillator strengths of aberrant atomic lines as necessary. We preferred the Sun over Arcturus in this process, given that Arcturus is cool giant with stronger molecular absorption features (e.g., the G band) that are more difficult to match. For features absent from the line list, which could not be resolved by considering lines with log $gf < -5$, we included Fe I transitions with EPs and log gf to match the observed strength in both the Sun and Arcturus. The final blue line list contains 132 chemical species (atomic, molecular, neutral, and ionized), including 74 unique elements and 2 molecules (CN and CH). In total, the line list contains 53,164 atomic line transitions and 58,062 molecular transitions.

Figure 1 illustrates a comparison between the Hinkle spectra and their syntheses for the Sun and Arcturus. At the expected resolution of the DEIMOS 600ZD grating (∼ 2.8 Å), the mean absolute deviation of the residuals between the observed spectra and their syntheses across the wavelength range of the line list are 8.3×10^{-3} and 2.2×10^{-2} for the Sun and Arcturus respectively.

4.2. *Synthetic Spectra*

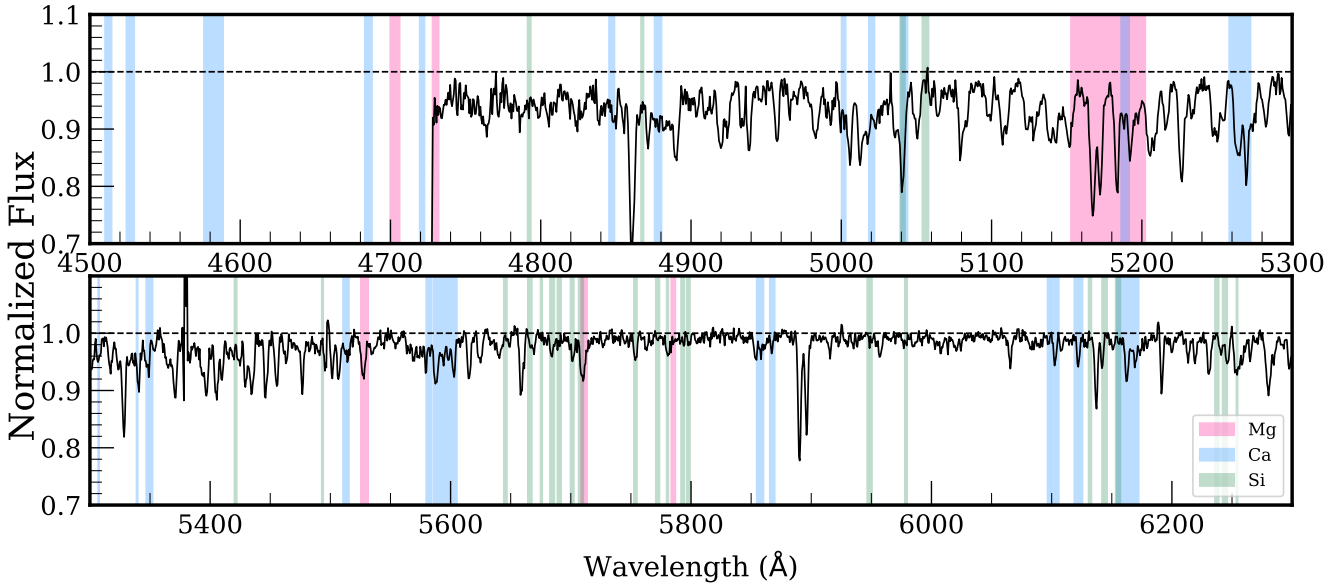

FIG. 2.— Wavelength regions sensitive to changes in [α/Fe] for the spectral resolution of the DEIMOS 600ZD grating ($\sim$ 2.8 Å). We show an example spectrum (*black*) over the wavelength range 4500 - 6300 Å, where we corrected the spectrum for telluric absorption (§ 3.1) and performed an initial continuum normalization (§ 3.3). We do not show spectral regions with wavelengths below 4500 Å, since low S/N generally prevents utilization of the observed spectrum in this wavelength range. The spectrum is for a star in the globular cluster NGC 2419. Spectral regions sensitive to Mg, Ca, and Si are shown as highlighted ranges in magenta, blue, and green respectively. The atmospheric value of [α/Fe] is measured using the union of the Mg, Ca, and Si spectral regions.

TABLE 4
PARAMETER RANGES OF BLUE GRID (4100 - 6300 Å)

Parameter	Minimum Value	Maximum Value	Step
T_{eff} (K)	3500	5600	100
	5600	8000	200
log g (cm s^{-2})	0.0 ($T_{eff} < 7000$ K)	5.0	0.5
	0.5 ($T_{eff} > 7000$ K)	5.0	0.5
[Fe/H]	–4.5[a] ($T_{eff} \leq 4100$ K)	0.0	0.1
	–5 ($T_{eff} > 4100$ K)	0.0	0.1
[α/Fe]	–0.8	1.2	0.1

[a]Below [Fe/H] < –4.5 for $T_{eff} \leq 4100$ K, certain stellar atmosphere models fail to converge when solving for molecular equilibrium in each atmospheric layer. Synthetic spectra with [Fe/H] < –4.5 exist for a majority of T_{eff}-log g pairs for $T_{eff} \leq 4100$ K, but our grid is complete for all parameter combinations only above [Fe/H] = –4.5 in this regime.

We employ the ATLAS9 (Kurucz 1993) grid of model stellar atmospheres, with no convective overshooting (Castelli et al. 1997). We base our grid on recomputed (Kirby et al. 2009 and references therein) ATLAS9 model atmospheres with updated opacity distribution functions, available for [α/Fe] = 0.0 and +0.4 (Castelli & Kurucz 2004). We adopt the solar composition of Anders & Grevesse 1989, except for Fe (Sneden et al. 1992). The elements considered to be α-elements are O, Ne, Mg, Si, S, Ar, Ca, and Ti.

For stellar parameters between grid points, we linearly interpolated to generate model atmospheres within the ranges 3500 K < T_{eff} < 8000 K, 0.0 < log g < 5.0, –4.5 < [Fe/H] < 0.0, and -0.8 < [α/Fe] < +1.2. A full description of the grid is presented in Table 4. Here, [α/Fe] represents a *total* α-element abundance for the atmosphere, which augments the abundances of individual α-elements without distinguishing between their relative abundances. In total, the grid contains 316,848 synthetic spectra.

We generated the synthetic spectra using MOOG (Sneden 1973), an LTE spectral synthesis software. MOOG takes into account neutral hydrogen collisional line broadening (Barklem et al. 2000; Barklem & Aspelund-Johansson 2005), in addition to radiative and Stark broadening and van der Waals line damping. The most recent version (2017) includes an improved treatment of Rayleigh scattering in the continuum opacity (Alex Ji, private communication). The resolution of each generated synthetic spectrum is 0.02 Å.

4.3. *Photometric Constraints*

To reduce the dimensionality of parameter space and to optimize our ability to find the global chi-squared minimum in the parameter estimation (§ 4.5), we constrained the effective temperature and surface gravity of the synthetic spectra by available photometry for red giant stars in our sample. The photometric effective temperature is estimated using a combination of the Padova (Girardi et al. 2002), Victoria-Regina (VandenBerg et al. 2006), and Yonsei-Yale (Demarque et al. 2004) sets of isochrones, assuming an age of 14 Gyr and an α-element abundance of 0.3 dex. If available, we also employed the Ramírez & Meléndez (2005) color temperature. We adopted a single effective temperature ($T_{\rm eff,phot}$) and associated uncertainty ($\sigma_{T_{\rm eff,phot}}$) from an average of the isochrone/color temperatures for each star.

We determined the photometric surface gravity in a similar fashion. However, no color-log g relation exists, so we could not include this additional source for the photometric surface gravity. Unlike the effective temperature, we did not solve for log g using spectral synthesis techniques, as the errors on the photometric surface gravity are negligible when the distance is known. Additionally, LRS and MRS spectra cannot effectively provide constraints on its value owing to the lack of ionized lines in the spectra. Thus, we held log g fixed in the abundance determination.

4.4. *[Fe/H] and [α/Fe] Regions*

In order to increase the sensitivity of the synthetic spectrum fit to a given abundance measurement, we constructed

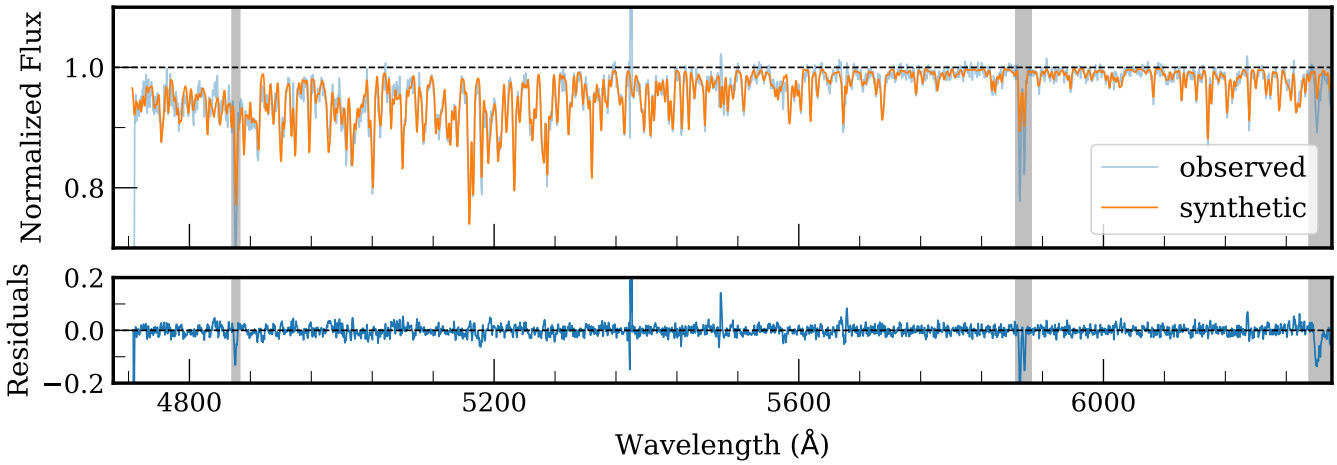

FIG. 3.— An example of a continuum-normalized observed spectrum (*light blue*) and its best-fit synthetic spectrum (*orange*). The observed spectrum corresponds to the same object in Figure 2. We show the portion of the fit utilizing our new blue grid of synthetic spectra ($\sim$ 4700 - 6300). The highlighted regions (*grey*) correspond to our standard mask (§ 3.4), which excludes lines such as Hβ, Na D1 and D2 from the fit. We adopt the parameters of the best-fit synthetic spectrum for the observed spectrum, $T_{\rm eff}$ = 4296 K, log g = 0.71 dex, [Fe/H] = -1.98 dex, [α/Fe] = 0.18 dex, and $\Delta\lambda$ = 2.66 Å FWHM. We measure χ^2_ν = 1.64 for the quality of the fit across the full wavelength range ($\sim$ 4700 - 9100 Å), based on the regions of the spectrum used to measure [Fe/H] (§ 4.4). The normalized residuals (*dark blue*) between the continuum-refined observed spectrum and best-fit synthetic spectrum are also shown. The residuals have been scaled by the inverse variance of the observed spectrum and the degree of freedom of the fit, such that each pixel represents the direct contribution to χ^2_ν.

wavelength masks that highlight regions that are particularly responsive to changes in [Fe/H] and [α/Fe]. We employed the same procedure as Kirby et al. (2009) to make the masks, starting with a base synthetic spectrum for each combination of $T_{\rm eff}$ (3500 - 8000 K in steps of 500 K) and log g (0.0 - 3.5 in steps of 0.5 dex). We assumed a bulk metallicity [Fe/H] = -1.5 and solar [α/Fe] for the atmosphere. We then generated synthetic spectra with either enhanced or depleted values of individual element abundances (Fe, Mg, Si, Ca, and Ti) for each $T_{\rm eff}$-log g pair and compare to the base synthetic spectra, identifying wavelength regions that differ by more than 0.5%. In the determination of the [Fe/H] and [α/Fe] wavelength regions, we smoothed all synthetic spectra used to an approximation of the expected resolution of the 600ZD grating ($\sim$ 2.8 Å) across the entire spectrum (4100 - 9100 Å). We then compared the spectral regions for each element against the line list and high signal-to-noise (S/N $>$ 100) spectra of cool ($T_{\rm eff}$ $<$ 4200 K) globular cluster stars, eliminating any regions that do not have a corresponding transition in the line list or an absorption feature in the spectra.

Although our measurements reflect the atmospheric value of [α/Fe], we constructed the associated wavelength mask from the regions sensitive to changes in the individual elements Mg, Si, and Ca. We excluded Ti from the [α/Fe] mask owing to the prevalence of regions sensitive to Ti at bluer optical wavelengths, such that we cannot meaningfully isolate its elemental abundance. Figure 2 illustrates our [α/Fe] mask in the blue (4500 - 6300 Å). The [Fe/H] spectral regions cover 92% and 51% of the wavelength range in the red and blue respectively, whereas the [α/Fe] regions span 15% and 12% of the same wavelength ranges. The overlap between the [Fe/H] regions and [α/Fe] regions is 16% and 23% in the blue and red respectively. We emphasize that [Fe/H] and [α/Fe] are measured separately and iteratively (§ 4.5).

4.5. *Parameter Determination from Spectral Synthesis*

Here, we outline the steps involved in our measurement of atmospheric parameters and elemental abundances from spectral synthesis of low-resolution spectra. Our method is nearly identical to that of Kirby et al. (2009), excepting our introduction of an additional free parameter, $\Delta\lambda$, the resolution of the observed spectrum. We use a Levenberg-Marquardt algorithm to perform each comparison between a given observed spectrum and a synthetic spectrum. We weight the comparison according to the inverse variance of the observed spectrum. In each step, the synthetic spectra utilized in the minimization are interpolated onto the observed wavelength array and smoothed to the fitted observed resolution, $\Delta\lambda$, prior to comparison with a given observed spectrum.

1. *T_{eff}, [Fe/H], and $\Delta\lambda$, first pass.* All three parameters are allowed to vary simultaneously in the fit. We use only regions sensitive to [Fe/H] (§ 4.4) in this measurement. We choose to measure $\Delta\lambda$ simultaneously with $T_{\rm eff}$ and [Fe/H] to prevent the chi-squared minimizer from under- or over-smoothing the synthetic spectrum to compensate for the initial guesses of $T_{\rm eff}$ and [Fe/H], which are offset from the final parameter values corresponding to the global χ^2 minimum. The [Fe/H] regions cover almost the entire spectrum (92%) in the wavelength range 4100 - 6300 Å and a majority of the spectrum (51%) in the range 6300 - 9100 Å, such that using the entire spectrum to measure $\Delta\lambda$ does not change the results within the statistical uncertainties.

   We assume a starting value of $T_{\rm eff,phot}$ (§ 4.3) for the spectroscopic effective temperature. $T_{\rm eff}$ is constrained by photometry using a Gaussian prior, such that χ^2 increases if $T_{\rm eff}$ deviates substantially from $T_{\rm eff,phot}$, as defined by the associated error in the photometric effective temperature ($\sigma_{T_{\rm eff,phot}}$). As motivated in § 4.3, log g is fixed at the photometric value in all steps. We initialize [Fe/H] at −2 dex, where we performed tests to ensure that the final value of [Fe/H] does not depend on the initial guess. Similar to the approach for $T_{\rm eff}$, we enforce a Gaussian prior with a mean of 2.8 Å and standard deviation of 0.05 Å on $\Delta\lambda$, according to the expected spec-

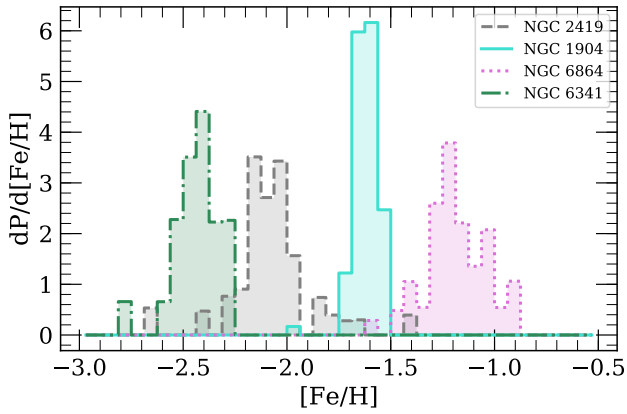

FIG. 4.— Error-weighted metallicity ([Fe/H]) distribution functions for RGB members of Galactic globular clusters NGC 2419 (*grey*), NGC 1904 (*cyan*), NGC 6864 (*magenta*), and NGC 6341 (*green*). Only stars for which δ[Fe/H] < 0.3 dex are shown. We find mean cluster metallicites of −2.08 dex, −1.63 dex, −1.19 dex, and −2.45 dex for the four respective clusters.

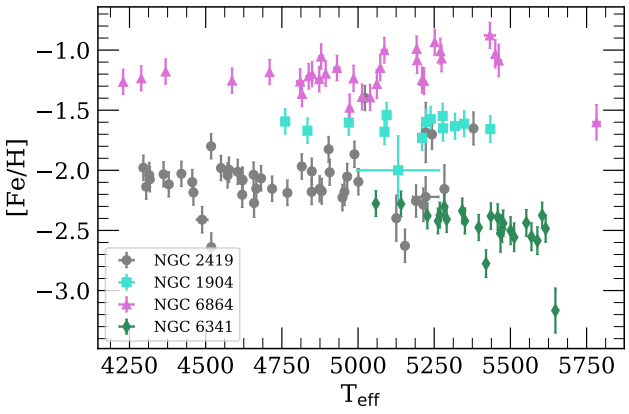

FIG. 5.— Metallicity ([Fe/H]) vs. spectroscopic effective temperature ($T_{\rm eff}$) for the same data set as Figure 4. The lack of a trend between the two quantities for each GC implies that our chemical abundance analysis is robust to systematic covariance in these parameters.

tral resolution for the 600ZD grating. [α/Fe] remains fixed at solar, whereas the other parameters are allowed to vary until the best-fit synthetic spectrum is found.

2. *[α/Fe], first pass.* $T_{\rm eff}$, [Fe/H], and $\Delta\lambda$ are fixed at the values determined in step 1 while [α/Fe] is allowed to vary, assuming a starting value of solar. In the determination of the best-fit synthetic spectrum, only wavelength ranges sensitive to variations in α-element abundance are considered (§ 4.4).

3. *Iterative continuum refinement.* After a best-fit synthetic spectrum is determined according to steps 1 and 2, we refine the continuum normalization according to § 3.3. We perform the continuum refinement iteratively, enforcing the convergence conditions that the difference in parameter values between the previous and current iteration cannot exceed 1 K, 0.001 dex, 0.001 dex, and 0.001 Å for $T_{\rm eff}$, [Fe/H], [α/Fe], and $\Delta\lambda$ respectively. If these conditions are not met in a given iteration, the continuum-refined spectrum is used to repeat steps 1 and 2 until convergence is achieved. If the maximum number of iterations ($N_{\rm iter,\,max}$ = 50) is exceeded, which occurs for a small fraction of observed spectra, we do not include the observed spectra in the subsequent analysis.

4. *[Fe/H], second pass.* [Fe/H] is redetermined, where $T_{\rm eff}$ and $\Delta\lambda$ are fixed at their converged values from step 3 and [α/Fe] = 0. We use the final continuum-refined observed spectrum determined in step 3 in this step and all remaining steps.

5. *[α/Fe], second and final pass.* We repeat step 2, holding [Fe/H] fixed at the value determined in step 4.

6. *[Fe/H], third and final pass.* We repeat step 4, holding [α/Fe] fixed at the value determined in step 5.

5. GLOBULAR CLUSTER VALIDATION TESTS

We demonstrate the robustness of our LRS technique by applying it to a set of MW GCs: NGC 2419, NGC 1904 (M79), NGC 6864 (M75), and NGC 6341 (M92).

NGC 2419 is a luminous outer halo GC located ∼ 90 kpc away from the Galactic center (Harris et al. 1997) with multiple stellar populations, but no detected variation in [Fe/H] (Cohen & Kirby 2012). NGC 6864 also exhibits evidence for chemically distinct populations, including a marginal spread in [Fe/H] (∼ 0.07 dex; Kacharov et al. 2013). It is a relatively young GC (Catelan et al. 2002) at a Galactocentric radius of ∼ 15 kpc (Harris et al. 1997). NGC 1904 (∼ 19 kpc; Harris et al. 1997) possesses an extended blue horizontal branch, but it is otherwise a typical cluster. NGC 6341 (∼ 9 kpc; Harris et al. 1997) is notable primarily for being very metal-poor ([Fe/H] ∼ −2.3 dex). For a summary of observations used in our validation tests, see Table 1.

5.1. *Membership*

For all subsequent analysis in this section, we utilize only stars that have been identified as RGB star members by Kirby et al. (2016). We removed asymptotic giant branch stars from our GC sample that Kirby et al. (2016) manually selected from color-magnitude diagrams. Membership is defined using both radial velocity and metallicity criteria based on MRS, such that any star whose measurement uncertainties are greater than 3σ from the mean of either radial velocity or metallicity is not considered a member. The colors and magnitudes of member stars must also conform to the cluster's giant branch.

5.2. *Metallicity*

As described in § 4.5, we measure metallicity from spectral regions sensitive to variations in [Fe/H]. In addition to membership criteria (§ 5.1), we further refine our sample by requiring that the 5σ contours in each of the four fitted parameters (§ 4.5) identify the minimum. This condition is effectively equivalent to requiring that a given star has sufficient S/N, a converged continuum iteration, and overall high enough quality fit (χ^2_ν) to produce a reliable abundance measurement.

We illustrate our results for [Fe/H] in the form of metallicity distribution functions (Figure 4) for NGC 2419, NGC 1904, NGC 6864, and NGC 6341, where we weight the distribution according to the *total* error in [Fe/H]. For a discussion of the measurement uncertainties, including systematic uncertainties, see § 7. We find that $\langle$[Fe/H]$\rangle$ = −2.08 ± 0.21 dex, −1.63 ± 0.07 dex, −1.19 ± 0.15 dex, and −2.45 ± 0.19

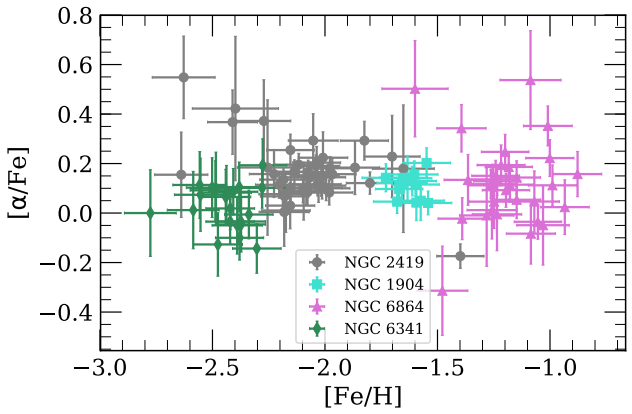

FIG. 6.— Atmospheric [α/Fe] versus [Fe/H] for the same data set as Figure 4, where we also exclude points with δ([α/Fe]) > 0.3 dex. There is no apparent anticorrelation between [α/Fe] and [Fe/H] within a GC, indicating that our method does not show any unphysical covariance between these two parameters.

dex for NGC 2419, NGC 1904, NGC 6864, and NGC 6341 respectively, where $\langle$[Fe/H]$\rangle$ is weighted according to the inverse variance of the total measurement uncertainty. These values agree with the corresponding quantities from HRS: -2.12 ± 0.09 (Cohen & Kirby 2012), -1.58 ± 0.03 (Carretta et al. 2009b), -1.16 ± 0.07 (Kacharov et al. 2013), and -2.34 dex (Sneden et al. 2000)[2] respectively. We present a detailed comparison to HRS abundances in § 6.

As another example of our ability to reliably recover [Fe/H], we show [Fe/H] vs. spectroscopically determined $T_{\rm eff}$ in Figure 5 for all GCs. In a nearly mono-metallic population like a GC, correlation of metallicity with other fitted parameters, such as $T_{\rm eff}$, would indicate the presence of systematic effects. Because $T_{\rm eff}$ is strongly covariant with [Fe/H], the fitting procedure might erroneously select a lower value of [Fe/H] and $T_{\rm eff}$ in order to match spectral features. Figure 5 presents evidence against any such correlation.

5.3. *α-element Abundance*

Similarly, we do not anticipate a correlation between [Fe/H] and [α/Fe] within a GC. [α/Fe] abundance impacts the determination of [Fe/H] via its contribution of H^- opacity to the stellar atmosphere through electron donation. Thus, the abundance of [α/Fe] alters stellar atmospheric structure, requiring a re-evaluation of [Fe/H] in the spectral fitting process. The presence of trends between [α/Fe] with [Fe/H] (e.g., increasing [α/Fe] with decreasing [Fe/H]) within a GC, which we expect to contain no such correlations, would indicate systematic effects in measuring abundances. As summarized in Figure 6, no such systematics are present in our data for each GC.

6. COMPARISON TO HIGH-RESOLUTION SPECTROSCOPY

6.1. *High-Resolution Data*

Given the variety in approaches of HRS studies of the MW GCs listed in Table 1, we provide a summary of the stellar parameter determination and abundance analysis in each case. For all GCs, membership is determined based on radial velocities.

[2] Sneden et al. (2000) do not cite random uncertainties on their abundances. We represent their [Fe/H] and [α/Fe] (§ 6) values as simple means.

- *NGC 2419*: Using Keck/HIRES ($R \sim 34{,}000$) spectroscopy, Cohen & Kirby (2012) measured [Fe/H], [Mg/Fe], [Si/Fe], and [Ca/Fe] for 13 RGB stars in NGC 2419. They used MOOG (Sneden 1973) in combination with Castelli & Kurucz (2004) atmospheric models to derive equivalent widths from neutral lines across the wavelength range 4500 - 8350 Å, including the Mg triplet. Stellar parameters were set to photometric values. Measurement uncertainties represent the dispersion of the mean abundance based on the various lines used in the abundance determination.

- *NGC 6864*: Kacharov et al. (2013) used Magellan/MIKE ($R \sim 30{,}000$) to observe 16 RGB stars in NGC 6864 over a wavelength range of 3340 - 9150 Å. They measured [Fe/H], [Mg/H], [Si/H], and [Ca/H] via equivalent width measurements using MOOG and Castelli & Kurucz (2004) atmospheric models. Mg was measured from a single line (5711 Å). They determined $T_{\rm eff}$ from excitation equilibrium and surface gravities from $T_{\rm eff}$, extinction-corrected bolometric magnitude, and the known distance to the cluster. The measurement uncertainties are a combination of the random error (based on the number of lines used in the abundance analysis for a given element) and a component that reflects the error from adopted stellar atmosphere parameters. For the latter component, we adopt the larger, more conservative errors that reflect averages based on the entire GC sample of Kacharov et al. (2013).

We emphasize that the HRS abundances do not include true estimates of systematic uncertainty, e.g., resulting from limitations from the selected grid of model atmospheres or line list. Additionally, we are comparing our homogenous LRS abundances to an inhomogenous HRS sample. As a result, some of the differences among the HRS studies can be attributed simply to different abundance measurement tools and techniques.

6.2. *Abundance Comparison*

We find reasonable agreement in [Fe/H] for the 9 stars common between both data sets, within the 1σ uncertainties. In order to perform the comparison, we have shifted the HRS abundances (Cohen & Meléndez 2005; Asplund et al. 2009) to the same solar abundance scale as the LRS abundances. Figure 7 shows no correlation between the LRS and HRS metallicity measurements within each of NGC 2419 and NGC 1904, which is expected for monometallic globular clusters.

In order to compare our [α/Fe] measurements to an analogous HRS quantity, we construct [α/Fe]$_{\rm HRS}$ based on a weighted sum of Mg, Si, and Ca elemental abundances. To derive the weights, we start with a reference synthethic spectrum defined by $T_{\rm eff}$ = 4400 K, log g = 1.0 dex, [Fe/H] = −1.8 dex, which correspond to mean parameter values from HRS studies of NGC 2419, NGC 1904, NGC 6864, and NGC 6341, and [α/Fe] = 0. We assume a spectral resolution of $\Delta\lambda$ = 2.8 Å and interpolate the synthetic spectrum onto a wavelength array with spacing equal to the pixel scale of the 600 line mm^{-1} grating ($\sim$ 0.64 Å). Next, we enhance/deplete the α-element abundance by 0.1, 0.2, and 0.3 dex, calculating the sum of the absolute difference between the reference and enhanced/depleted synthetic spectrum in each case. For each α-element, we utilize only the relevant wavelength regions

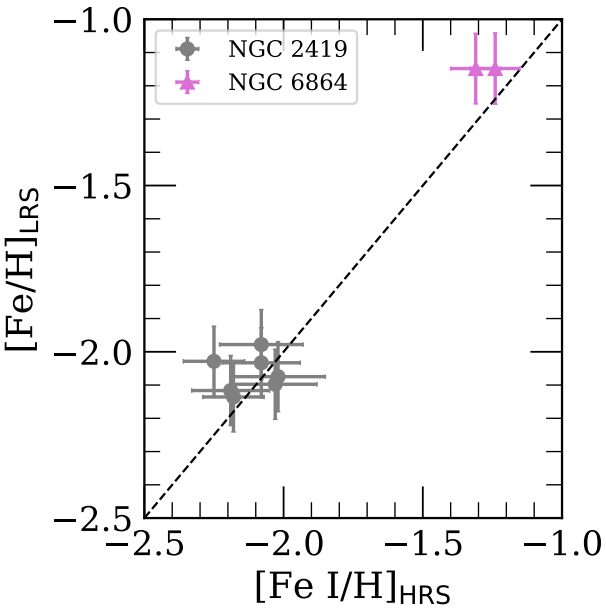

FIG. 7.— Metallicity measured from LRS ([Fe/H]) versus HRS ([Fe I/H]) (Cohen & Kirby 2012; Kacharov et al. 2013) for NGC 2419 and NGC 6864. Between LRS and HRS data sets, we have common measurements for 9 stars. Although some scatter is present between data sets, they exhibit broad agreement within the 1σ uncertainties ($\delta\epsilon_{\rm sys} = 0.02$ dex, Eq. 3). No correlation exists between the LRS and HRS measurements, which we expect for a monometallic GC.

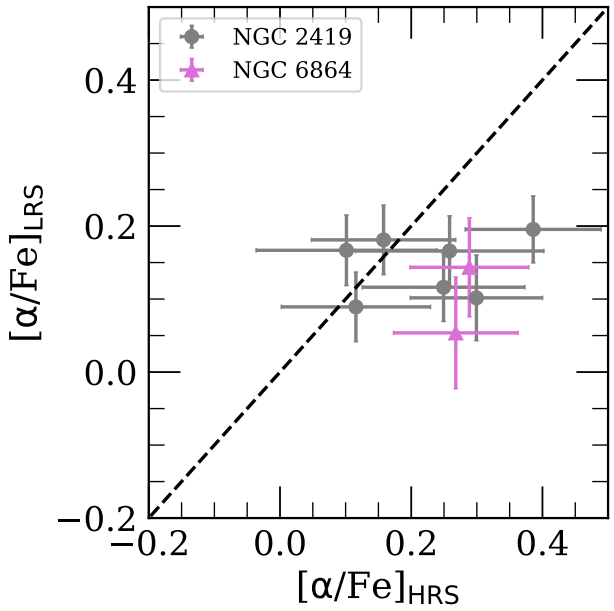

FIG. 8.— $[\alpha/{\rm Fe}]_{\rm HRS}$ versus $[\alpha/{\rm Fe}]_{\rm LRS}$ for NGC 2419 and NGC 1904. We construct $[\alpha/{\rm Fe}]_{\rm HRS}$ based on a weighting (§ 6.2) of its individual α-element abundances. The LRS and HRS abundances exhibit broad agreement ($\delta\epsilon_{\rm sys}$ consistent with zero, Eq. 3), despite the intrinsic differences between the sets of measurements.

(§ 4.4) and spectral coverage that corresponds to our data set (4500 - 9100 Å). Additionally, we exclude contributions from masked wavelength regions (§ 3.4). We adopt the normalized average value of the summed absolute flux differences as our final weight for a given element, i.e.,

$$[\alpha/{\rm Fe}]_{\rm HRS} = 0.282 \times [{\rm Mg/Fe}]_{\rm HRS} + 0.136 \times [{\rm Si/Fe}]_{\rm HRS} + 0.582 \times [{\rm Ca/Fe}]_{\rm HRS}, \quad (1)$$

$$\delta[\alpha/{\rm Fe}]_{\rm HRS} = \Big[\big(0.282 \times \delta[{\rm Mg/Fe}]_{\rm HRS}\big)^2 + \big(0.136 \times \delta[{\rm Si/Fe}]_{\rm HRS}\big)^2 + \big(0.582 \times \delta[{\rm Ca/Fe}]_{\rm HRS}\big)^2\Big]^{1/2}. \quad (2)$$

In Figure 8, we utilize Eqs. 1 and 2 to directly compare HRS and LRS α-element abundances in NGC 2419 and NGC 6864. We emphasize that $[\alpha/{\rm Fe}]_{\rm HRS}$ represents only an approximation to the atmospheric value of $[\alpha/{\rm Fe}]$, given the fundamental differences between the HRS and LRS methods (§ 6.1).

In Table 5, we summarize our findings for $\langle[\alpha/{\rm Fe}]\rangle_{\rm LRS}$ in MW GCs and compare to equivalent HRS measurements constructed using Eqs. 1 and 2. In the case of NGC 6341, we construct $[\alpha/{\rm Fe}]_{\rm HRS}$ based only on [Ca/Fe] and [Si/Fe] because Sneden et al. (2000) did not measure [Mg/Fe]. We renormalized the weights in Eqs. 1 and 2 accordingly. The average LRS α-element abundances are lower than the HRS measurements by ~ 0.1 - 0.15 dex, excepting the case of NGC 6341. We find a significantly lower value of $\langle[\alpha/{\rm Fe}]\rangle$, although we note that it is particularly difficult to compare between LRS and HRS in this case, given that NGC 6341 lacks Mg abundances.

TABLE 5
$\langle[\alpha/{\rm Fe}]\rangle$ IN MW GCS

GC	$\langle[\alpha/{\rm Fe}]_{\rm LRS}\rangle$ (dex)	$\langle[\alpha/{\rm Fe}]_{\rm HRS}\rangle$ (dex)
NGC 2419	0.13 ± 0.09	0.21 ± 0.09
NGC 1904	0.11 ± 0.05	0.28 ± 0.02
NGC 6864	0.13 ± 0.11	0.28 ± 0.07
NGC 6341	0.03 ± 0.09	0.37

Note.— The HRS references for NGC 2419, NGC 1904, NGC 6864, and NGC 6341 are Cohen & Kirby (2012), Carretta et al. (2009b, 2010), Kacharov et al. (2013), and Sneden et al. (2000), respectively.

Despite this apparent offset in the cluster means, we find that a star-by-star comparison of [α/Fe] and [Fe/H] shows that our LRS results are consistent with those from HRS within the random uncertainties. We prove this consistency by calculating what additional error term would be required to force the LRS and HRS measurement to agree within one standard deviation. The relevant equation is

$$\frac{1}{N}\sum_{i}^{N} \frac{\big(\epsilon_{\rm LRS,i} - \epsilon_{\rm HRS,i}\big)^2}{\big(\delta\epsilon^2_{\rm LRS,i} + \delta\epsilon^2_{\rm HRS,i} + \delta\epsilon^2_{sys}\big)} = 1, \quad (3)$$

where ϵ represents a given elemental abundance, such as [Fe/H] or [α/Fe], $\delta\epsilon$ is the corresponding statistical uncertainty on the measurement, i is an index representing a given star in common between both the HRS and LRS data sets, and N is the total number of common stars. We do not find a solution for $\delta\epsilon_{\rm sys}$ in the case of [α/Fe], indicating that, even without a systematic component, the measurements are consistent. For the case of [Fe/H], we find $\delta\epsilon_{\rm sys} = 0.02$, which is negligible. Thus, upon inclusion of our systematic uncertainties determined from intrinsic dispersion in GCs (§ 7), $[{\rm Fe/H}]_{\rm LRS}$ and $[\alpha/{\rm Fe}]_{\rm HRS}$ agree with the HRS data within 1σ.

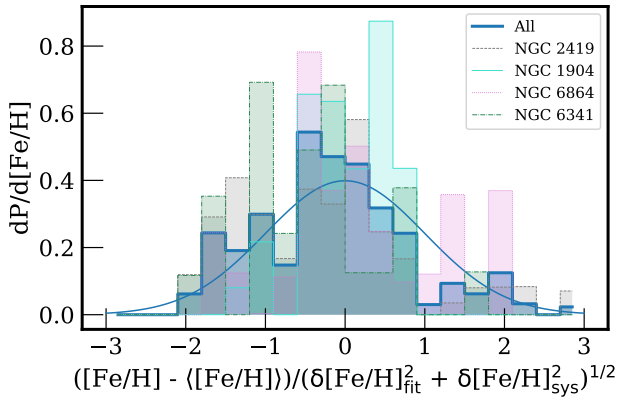

FIG. 9.— Probability distribution function of [Fe/H] normalized to the mean metallicity of a given cluster ($\langle$[Fe/H]$\rangle$) and weighted by the total error in metallicity. We show the distributions for NGC 2419 (*grey*), NGC 1904 (*cyan*), NGC 6864 (*magenta*), NGC 6341 (*green*), and all four clusters (*blue*) (117 stars). The total error is composed of the statistical uncertainty from the fit (δ[Fe/H]$_{\rm fit}$) and the systematic uncertainty (δ[Fe/H]$_{\rm sys}$). We determine the systematic uncertainty from the intrinsic dispersion in the combined distribution for all three clusters. The Gaussian defined by the systematic uncertainty (δ([Fe/H])$_{\rm sys}$ = 0.105) is overplotted.

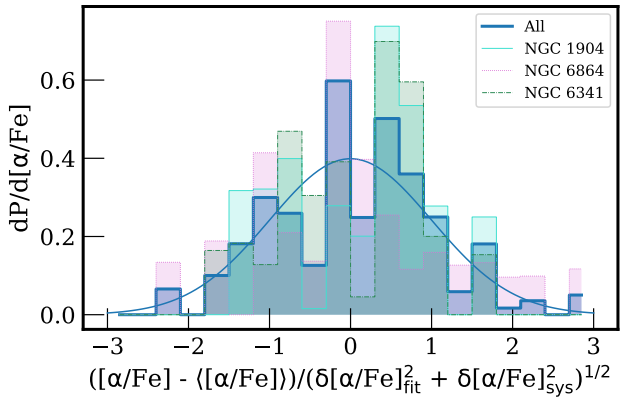

FIG. 10.— Probability distributions used to determine the systematic uncertainty, as in Figure 9, except for the case of [α/Fe]. We show the distributions for NGC 1904 (*cyan*), NGC 6864 (*magenta*), NGC 6341 (*green*), and all three clusters (*blue*) (69 stars). We find that δ([α/Fe])$_{\rm sys}$ = 0.039 dex.

TABLE 6
SYSTEMATIC UNCERTAINTY

Parameter	$\delta_{\rm sys}$ (dex)	$N_\star$[a]
[Fe/H]	0.105	117
[α/Fe]	0.039	69

[a]Number of stars used to determine the systematic uncertainty.

7. QUANTIFICATION OF SYSTEMATIC UNCERTAINTY

The total uncertainty on fitted parameters is composed of two components added in quadrature, the statistical (fit) uncertainty, $\delta_{\rm fit}$, and a systematic component, $\delta_{\rm sys}$. The fit uncertainty is calculated according to the reduced chi-squared value (χ^2_ν) and the diagonals of the covariance matrix of the fit (σ_{ii}), i.e., $\sigma_{ii}(\chi^2_\nu)^{1/2}$. We calculate χ^2_ν using only the regions of the observed spectrum utilized in the fit, e.g., in the case of [Fe/H], we use the wavelength regions sensitive to [Fe/H] (§ 4.4) and not excluded by the pixel mask (§ 3.4). The systematic component encapsulates uncertainty intrinsic to our method, owing to sources such as the linelist (§ 4.1), assumptions involved in spectral synthesis (§ 4.2), details of our method, such as the continuum normalization (§ 3.3) and fitting procedure (§ 4.5), and covariance with other fitted parameters.[3]

7.1. *Metallicity*

Because most GCs, including those in our sample, are nearly monometallic (Carretta et al. 2009a), we can derive an estimate of systematic uncertainty in [Fe/H], δ[Fe/H]$_{\rm sys}$, by enforcing the condition that the intrinsic dispersion in the GC is zero, i.e.,

$$\sigma^2 = {\rm var}\left[\frac{{\rm [Fe/H]_i} - \langle{\rm [Fe/H]}\rangle}{\left(\delta{\rm [Fe/H]}^2_{\rm fit,i} + \delta{\rm [Fe/H]}^2_{\rm sys}\right)^{1/2}}\right] = 1, \quad (4)$$

where i is the index for a star in the GC, δ[Fe/H]$_{\rm fit}$ is the S/N-dependent statistical uncertainty in [Fe/H], and $\langle$[Fe/H]$\rangle$ is the mean metallicity of the GC, where the mean is weighted by the statistical uncertainty on each measurement of [Fe/H]. Eq. 4 follows a reduced chi-squared distribution with an expectation value of unity. Enforcing the condition $\sigma^2 = 1$, we can numerically solve for the most likely value of the systematic uncertainty.

First, we refine our sample by removing outliers in [Fe/H] for each GC. Following Kirby et al. (2016), we calculate the mean metallicity, $\langle$[Fe/H]$\rangle$, and standard deviation, σ([Fe/H]), for each cluster, and we remove stars that deviate by more than 2.58σ (99% confidence level). Then, we re-compute $\langle$[Fe/H]$\rangle$ and σ([Fe/H]) from this refined sample, including only stars from the full sample that fulfill the criteria $|{\rm [Fe/H]} - \langle{\rm [Fe/H]}\rangle| - \delta({\rm [Fe/H]})_{\rm stat} < 3\sigma$. The inclusion of δ([Fe/H])$_{\rm stat}$ in the inequality allows stars to be considered members even if they fall outside of the allowed metallicity range, as long as some part of their 1σ confidence intervals falls within the range.

After performing this sigma clipping for each individual cluster, we subtract the mean cluster metallicity from each star's measurement of [Fe/H], and we solve for the intrinsic dispersion based on the combined sample (Eq. 4). We obtain a systematic uncertainty in [Fe/H] of δ[Fe/H]$_{\rm sys}$ = 0.105 dex (Table 6) based on 117 stars. We present an illustration of this method in Figure 9, where we show the probability distributions for the total-error-weighted metallicity of each cluster, in addition to the the combined GC sample. The fact that the combined distribution is well-approximated by a Gaussian with σ = 1 indicates that the calculated systematic uncertainty sufficiently accounts for the observed metallicity spread.

Thus, the total error is,

$$\delta{\rm [Fe/H]}_{\rm tot} = \sqrt{\delta{\rm [Fe/H]}^2_{\rm fit} + \delta{\rm [Fe/H]}^2_{\rm sys}} \quad (5)$$

In general, the statistical fit uncertainty is negligible compared

[3] We do not completely characterize the systematic uncertainty on $T_{\rm eff}$ and $\Delta\lambda$ because our primary goal is to determine abundances. The systematic errors δ([Fe/H])$_{\rm sys}$ and δ([α/Fe])$_{\rm sys}$ already account for errors propagated by inaccuracies in $T_{\rm eff}$ and $\Delta\lambda$. All of the of uncertainties in $T_{\rm eff}$ and $\Delta\lambda$ presented in this paper reflect only the statistical uncertainty.

TABLE 7
M31 Stellar Halo Observations

Object	Date	θ_s (")	$\langle X \rangle$	t_{exp} (s)	N
f130_2a	2018 Jul 19	1.0	1.53	5639	37
f130_2b[a]	2018 Jul 19	1.0	1.16	5758	37
f130_2a	2018 Aug 14	0.86	1.29	4140	37
f130_2a	2018 Oct 10	0.83	1.84	3000	37
f130_2a	2018 Oct 11	0.60	1.49	2400	37

[a]Slitmasks indicated "a" and "b" are identical, except that the slits are titled according to the median parallactic angle at the approximate time of observation.

to the systematic error for GCs. However, this will not be the case for M31, given the low value of the expected S/N.

7.2. *α-element Abundance*

To determine the systematic uncertainty in [α/Fe], $\delta([\alpha/\mathrm{Fe}])_{\mathrm{sys}}$, we calculate the intrinsic dispersion in the clusters, analogously to Eq. 4. Whereas it is generally reasonable to assume that GCs have negligible spread in [Fe/H], the assumption of zero intrinsic variation in [α/Fe] must be evaluated individually for each cluster. We exclude NGC 2419 from our combined GC sample in this case, given that abundance analysis of HRS has detected a significant spread in Mg (Cohen et al. 2011; Cohen & Kirby 2012). Although NGC 6864 possesses chemically distinct populations, O is the only α-element that exhibits significant variation within the cluster, as opposed to Mg, Si, or Ca (Kacharov et al. 2013). NGC 6341 is not known to possess α-element variations (Sneden et al. 2000), with the caveat that no recent Mg abundances from HRS have been published to our knowledge. We therefore construct our combined GC sample from NGC 1904, NGC 6864, and NGC 6341 to compute $\delta([\alpha/\mathrm{Fe}])_{\mathrm{sys}}$, obtaining a value of 0.039 dex (Table 6) from 69 stars. Figure 10 illustrates that the adopted error floor in [α/Fe] describes the data well. We anticipate a smaller value of $\delta([\alpha/\mathrm{Fe}])_{\mathrm{sys}}$ relative to $\delta([\mathrm{Fe/H}])_{\mathrm{sys}}$, given that the systematic effects (uncertainties in the line list, atmospheric parameters, continuum normalization, etc.) that impact [Fe/H] tend to similarly affect [α/H]. Therefore, the net effect on the [α/Fe] ratio is zero to first order.

8. THE STAR FORMATION HISTORY OF THE STELLAR HALO OF M31

We apply our spectral synthesis technique to spectra of individual RGB stars in the stellar halo of M31. We select a field with no identified substructure as an example. We will apply our method to additional stellar halo fields in future work.

8.1. *Halo Field Observations*

The field, f130_2, is located at 23 kpc in projected radius along the minor axis of M31, and was first observed and characterized by Gilbert et al. (2007) using the Keck II/DEIMOS 1200 line mm^{-1} grating. We selected it owing to its proximity to the 21 kpc halo field of Brown et al. (2007), for which Brown et al. (2009) presented catalogs of deep optical photometry obtained using the Advanced Camera for Surveys (ACS) on the *Hubble Space Telescope*.

Table 7 summarizes our observations of the M31 stellar halo field, which we observed with the same configuration as described in § 2. The total exposure time was 5.8 hours. Following Cunningham et al. (2016), we designed two separate slitmasks for the single field, with the same mask center, mask position angle, and target list, but with differing slit position angles. Switching slitmasks in the middle of the observation allows us to approximately track the change in parallactic angle over the course of the night. This technique mitigates flux losses due to differential atmospheric refraction (DAR), which disproportionately affects blue wavelengths. Thus, it is especially important to consider DAR when observing with the 600 line mm[1] grating, which covers a wider spectral range than any other DEIMOS grating.

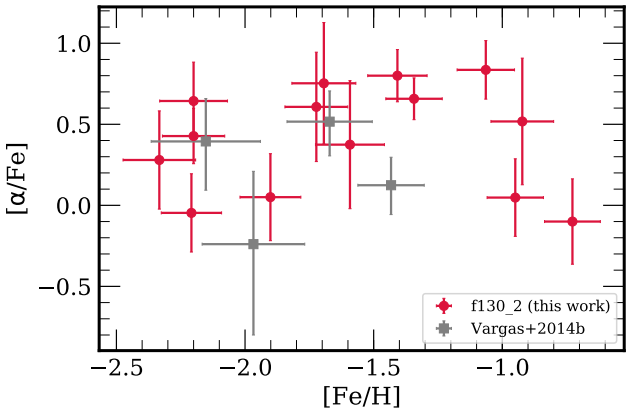

FIG. 11.— [α/Fe] vs. [Fe/H], measured from LRS, for M31 RGB stars (*red*) from a 23 kpc field with no identified substructure. We show a subset of our entire sample, with δ([Fe/H]) < 0.5 dex and δ([α/Fe]) < 0.5 dex, considering only stars with reliable abundance measurements. In total, we present [α/Fe] measurements for 14 M31 halo stars, substantially increasing the previous sample size of 4 stars (Vargas et al. 2014b). We plot the latter sample of metal-poor halo stars (*grey*) (S/N $\gtrsim$ 15 Å^{-1}) over our data set for comparison (S/N $\sim$ 8–22 Å^{-1}).

8.2. *Sample Selection*

The observed field, at a M31 galactocentric radius of 23 kpc, includes a non-negligible contamination fraction of Milky Way foreground dwarf stars. In order to identify secure M31 members, we used a likelihood-based method (Gilbert et al. 2006) that relies on three criteria to determine membership: the strength of the Na I λλ8190 absorption line doublet, the *(V, I)* color-magnitude diagram location, and photometric versus spectroscopic (Ca II λλ8500) metallicity estimates. Following Gilbert et al. (2007), we excluded radial velocity as a criterion to result in a more complete sample. In total, we identified 37 M31 stellar halo members ($20 \lesssim I_0 \lesssim 22.5$) in this field out of 106 targets.

We required that our abundance measurement technique determined the abundances reliably (§ 5.2): δ([Fe/H]) < 0.5 and $\delta([\alpha/\mathrm{Fe}]) < 0.5$. We also required that the 5σ χ^2 contours in each of the four fitted parameters (§ 4.5) identify the minimum. Both of these criteria effectively mimic a S/N cut (S/N $\gtrsim$ 8 Å^{-1}). Lastly, we manually screened member stars for molecular TiO bands between 7055–7245 Å (Cenarro et al. 2001; Gilbert et al. 2006), where affected stars exhibit a distinctive pattern. Stars with strong TiO absorption tend to be more metal-rich ([Fe/H] $\gtrsim -1.5$), have red colors ($(V-I)_0 > 2.0$), and can also show unusual χ^2 contours in [α/Fe]. We omitted 3 M31 member stars that meet the $(V-I)_0$ color criterion and show spectral evidence of strong TiO absorption. In total, this reduces the sample size to 14 stars (S/N $\sim$ 8–22 Å^{-1}), for which we present a summary of stellar parameters and chemical abundances in Table 8.

TABLE 8
PARAMETERS OF 14 M31 RGB STARS

Object	T_{eff}[a](K)	log g (dex)	[Fe/H] (dex)	[α/Fe] (dex)	$\Delta\lambda$[a](Å)	S/N (Å^{-1})
1282152	4050 ± 18	0.62	-0.95 ± 0.11	0.05 ± 0.24	2.88 ± 0.12	9
1282178	4338 ± 7	0.39	-2.33 ± 0.14	0.28 ± 0.30	2.79 ± 0.04	18
1291851	4453 ± 6	0.77	-2.20 ± 0.13	0.64 ± 0.24	2.81 ± 0.03	13
1292468	3793 ± 4	0.67	-0.92 ± 0.12	0.52 ± 0.39	2.74 ± 0.03	9
1292496	4369 ± 4	0.70	-0.73 ± 0.11	-0.10 ± 0.26	2.90 ± 0.02	17
1292507	3896 ± 5	0.46	-1.72 ± 0.12	0.61 ± 0.34	2.70 ± 0.05	13
1302682	4063 ± 5	0.85	-1.41 ± 0.12	0.80 ± 0.16	2.78 ± 0.03	14
1302710	4262 ± 9	1.07	-1.59 ± 0.13	0.37 ± 0.40	2.84 ± 0.04	8
1302971	3857 ± 3	0.53	-1.69 ± 0.12	0.75 ± 0.37	2.80 ± 0.04	10
1303039	4144 ± 4	0.52	-2.21 ± 0.12	-0.05 ± 0.24	2.83 ± 0.02	17
1303114	3749 ± 2	0.51	-1.06 ± 0.11	0.84 ± 0.18	2.89 ± 0.02	15
1303200	4337 ± 4	0.88	-1.90 ± 0.12	0.05 ± 0.27	2.83 ± 0.02	20
1303382	4356 ± 3	0.78	-2.20 ± 0.12	0.43 ± 0.17	2.81 ± 0.02	22
1303502	3906 ± 3	0.39	-1.34 ± 0.11	0.66 ± 0.13	2.91 ± 0.03	18

[a] As discussed in § 7, the errors presented for T_{eff} (and $\Delta\lambda$) represent only the random component of the total uncertainty.

8.3. *Results and Interpretation*

Our 14 measurements substantially increase the previous sample size for [α/Fe] measurements in the stellar halo of M31 from 4 stars (Vargas et al. 2014b). For our field, we find inverse-variance weighted values of $\langle$[Fe/H]$\rangle$ = −1.53 dex (for a comparison to previous work, see Appendix A), σ([Fe/H]) = 0.52 dex, $\langle$[α/Fe]$\rangle$ = 0.49 dex, and σ([α/Fe]) = 0.31 dex for our uniform, α-enhanced halo field at 23 kpc.

In addition to our 14 measurements of [α/Fe] and [Fe/H], Figure 11 includes the 4 outer halo stars from Vargas et al. (2014b) for comparison. Vargas et al. (2014b) utilized Gilbert et al.'s (2012) sample of M31 halo stars to identify stars within existing M31 dSph fields (Vargas et al. 2014a) for deeper spectroscopic follow-up. They narrowed their sample by enforcing the criteria that the stars were high-likelihood M31 members with S/N sufficient to measure abundances from MRS (S/N $\gtrsim$ 15 Å^{-1}). Their finalized sample originates from the metal-poor outer halo of M31 between ∼70 − 140 kpc. We re-compute the inverse-variance weighted average elemental abundances from their data, finding $\langle$[Fe/H]$\rangle$ = −1.70 dex, σ([Fe/H]) = 0.27 dex, $\langle$[α/Fe]$\rangle$ = 0.28 dex, and σ([α/Fe]) = 0.22 dex. In contrast to our work, Vargas et al. (2014b) applied an empirical correction factor to convert between the measured, atmospheric value of [α/Fe] and the average [α/Fe] calculated from individual α-element abundances.

As expected for a smooth halo field, we do not find evidence for a trend of [α/Fe] as a function of [Fe/H], in contrast to the expected abundance pattern (decreasing [α/Fe] with [Fe/H]) for fields dominated by a single, recent accretion event (such as the Giant Southern Stream; Ibata et al. 2001) or dwarf galaxies. Additionally, the fact that our [α/Fe] measurements at 23 kpc are consistent with those at ∼70–140 kpc (Figure 11) over the same metallicity range (−2.5 dex $\lesssim$ [Fe/H] $\lesssim$ −1.5 dex) suggests the lack of a significant radial trend with [α/Fe] in M31 stellar halo fields absent of substructure. We also find that our 23 kpc field is on average 0.2 dex more metal rich than the outer halo Vargas et al. (2014b) measurements (see Appendix A for a discussion of potential selection effects). In combination with the approximately constant value of [α/Fe] with both [Fe/H] and radius, this may indicate that we are probing the same extended halo component, which is metal-poor, α-enhanced, and underlies substructure at all radii (Chapman et al. 2006; Gilbert et al. 2012; Ibata et al. 2014).

Given the low luminosity of the smooth halo component (L $\sim 1.9\times10^8$ L$_\odot$ for [Fe/H]$_{phot}$ < −1.1 dex), Ibata et al. (2014) inferred that it would consist of many low luminosity structures accreted at early times. In terms of star formation history (SFH), high α-element abundances indicate that the stellar population in f130_2 is characterized by rapid star formation and is dominated by the yields of Type II supernovae. Recognizing that the outer regions ($\gtrsim$ 20 kpc) of the stellar halo are most likely formed via accretion (Johnston et al. 2008; Cooper et al. 2010; Tissera et al. 2012), we infer that the disrupted dwarf galaxies that were the progenitors of this field likely had short SFHs. Their SFHs could have been truncated by accretion onto M31.

Interestingly, the slightly lower average α-element abundance (0.28 dex) of Vargas et al. (2014b) could suggest that the outer halo is composed of progenitors with more extended chemical evolution as compared to the inner halo. If true, this would be in accordance with expectations from hierarchical buildup of the stellar halo (Johnston et al. 2008; Font et al. 2008). However, we cannot draw a robust conclusion on this matter given that the average α-element abundances, similar to the case of [Fe/H], between Vargas et al.'s 2014b sample and our sample are consistent at the 1σ level, which is compounded by limited sample sizes.

Our inferred SFH for f130_2 qualitatively agrees with the trend derived from deep photometry in a nearby *HST*/ACS field located at 21 kpc along the minor axis. The mask centers of the fields are separated by 6.33 arcmin on the sky, or 1.44 kpc, assuming a distance to both fields of 783 kpc (Stanek & Garnavich 1998). Using the Brown et al. (2006) method of comparing theoretical isochrones to color-magnitude diagrams, Brown et al. (2007) derived a SFH for the ACS field, assuming [α/Fe] = 0. They found a wide range of stellar ages and metallicities, providing support for an accretion origin, as opposed to early monolithic collapse. The field exhibits evidence for an extended SFH, with the majority of stellar ages between ∼8–10 Gyr, with a small but non-negligible ($\lesssim$ 5%) population of stars with ages $\lesssim$ 8 Gyr. The wide range of metallicity (−2.3 < [Fe/H] < −0.7 dex) that we find in this work is consistent with a multiple progenitor hypothesis. If the nearby ACS field is representative of f130_2, this implies a composition for f130_2 of intermediate-age system(s) that had elevated star formation rates, quenched at latest $\lesssim$ 8 Gyr ago.

Comparing our average α-element abundance to that of other systems, we find that, in general, they are similarly α-

enhanced. $\langle$[α/Fe]$\rangle$ for the 23 kpc M31 halo field agrees with that of M31 GCs (0.37 ± 0.16 dex) within 20 kpc of the galactic center (Colucci et al. 2009). Additionally, the metal-poor MW halo possesses elevated α-element abundance ratios of approximately +0.4 dex (Venn et al. 2004; Cayrel et al. 2004; Ishigaki et al. 2012; Bensby et al. 2014), which is comparable to our result.

Drawing comparisons to M31 dwarf galaxies is less straightforward, given that their average α-element abundance varies from approximately solar to highly α-enhanced ($\sim$0.5 dex) (Vargas et al. 2014a). This may indicate a range of star formation timescales for these systems, where some are dominated by old stellar populations ($\gtrsim$ 10 Gyr ago) and others possess intermediate-age ($\sim$10-7 Gyr ago) stars, although the systematic uncertainties on their SFHs at early times are large (Weisz et al. 2014). Vargas et al. (2014a) also found M31 dwarf galaxies to vary in terms of their internal [α/Fe] vs. [Fe/H] abundance patterns, ranging from constant (e.g., And VII; Tollerud et al. 2012) to decreasing [α/Fe] with respect to [Fe/H] (And V; Tollerud et al. 2012). The latter case is in accordance with abundance trends found in MW dwarf spheroidal galaxies (Shetrone et al. 2001, 2003; Tolstoy et al. 2003; Venn et al. 2004; Kirby et al. 2009, 2011a) and systems with more extended SFHs.

In terms of α-enhancement and SFH, our field resembles old M31 dSphs, although it is possible that f130_2 contains intermediate age stars (Brown et al. 2007). Vargas et al. (2014a) inferred that a present-day stellar halo constructed from M31 dwarf galaxies would be metal-rich, where $\langle$[Fe/H]$\rangle \sim -0.7$ dex (-1.4 dex) for their full sample (old dwarf galaxies only), with a distinct α-element abundance pattern as compared to the MW halo. Given the similarly flat [α/Fe]-[Fe/H] trend between f130_2 and And VII, and the similar $\langle$[Fe/H]$\rangle$ and [Fe/H] range between f130_2 and old M31 dSphs, it is possible that the progenitors of f130_2 were composed of systems similar to And VII. In order to meaningfully test if systems similar to present day M31 dwarf galaxies could have contributed to the smooth halo component, or whether the α-element abundance pattern of the smooth halo differs from that of the MW, we would require larger sample sizes across more halo fields.

9. SUMMARY

In an effort to increase the amount of available high-quality data in M31, we have developed a method of measuring [Fe/H] and [α/Fe] from low-resolution spectroscopy of individual RGB stars. We applied our technique to a field in M31's smooth stellar halo component.

The primary advantages of utilizing low-resolution spectroscopy are (1) the substantial increase in wavelength coverage (from $\sim$ 2800 Å with MRS to $\sim$ 4600 Å with LRS) available to constrain the abundances and (2) the accompanying increase in S/N per pixel for the same exposure time and observing conditions. To make spectral synthesis of DEIMOS LRS a reality, we generated a new grid of synthetic spectra spanning 4100 − 6300 Å based on a line list we constructed for bluer optical wavelengths. We find the following results:

1. Testing our technique on Galactic GCs, we do not find evidence for any systematic covariance between fitted parameters, such as $T_{\rm eff}$ and [Fe/H]. In light of the the fundamental inhomogeniety of the various HRS samples compared to our LRS data set, our measurements broadly agree with HRS abundances.
2. Based on the intrinsic dispersion in [Fe/H] and [α/Fe] of Galactic GCs with no known abundance variations in Fe, Mg, Ca, or Si, we estimate error floors of $\delta([{\rm Fe/H}]_{\rm sys} = 0.105$ dex and $\delta([\alpha/{\rm Fe}]_{\rm sys} = 0.039$ dex.
3. We present measurements for 14 RGB stars of [Fe/H] *and* [α/Fe] in the stellar halo of M31, tripling the previous sample size of 4 stars. The field has no identified substructure and is located at 23 kpc in galactocentric projected radius. We find that $\langle$[Fe/H]$\rangle = -1.53 \pm 0.52$ dex and $\langle[\alpha/{\rm Fe}]\rangle = 0.49 \pm 0.31$ dex for this field.
4. $\langle$[α/Fe]$\rangle$ agrees with the value of the MW halo plateau ($\sim$0.4 dex), M31 GCs, and some α-enhanced M31 dwarf galaxies. Our measurements exhibit overlap with previously published [α/Fe] measurements for M31 halo RGB stars at larger projected radii (70−140 kpc), showing no evidence for a significant radial trend in [α/Fe] in our limited sample.
5. Given its high α-enhancement, we surmise that the smooth halo field is likely composed of disrupted dwarf galaxies with elevated star formation rates and truncated SFHs, accreted early in the formation history of M31.

In future work, we will measure [Fe/H] and [α/Fe] from $\sim$6 hour observations of individual RGB stars in additional M31 halo and tidal stream fields with deep *HST* photometry (Brown et al. 2006), with the goal of deriving chemically-based star formation histories.

The authors thank Alis Deason for assistance in line list vetting, Gina Duggan for useful discussions on generating grids of synthetic spectra, Raja Guha Thakurta for help with observations and insightful conversations, and Luis Vargas and Marla Geha for sharing their data for M31 outer halo RGB stars. IE acknowledges support from a Ford Foundation Predoctoral Fellowship and the NSF Graduate Research Fellowship under Grant No. DGE-1745301, as well as the NSF under Grant No. AST-1614081, along with ENK. KMG. and JW acknowledge support from NSF grant AST-1614569. ECC was supported by a NSF Graduate Research Fellowship as well as NSF Grant No. AST-1616540. The analysis pipeline used to reduce the DEIMOS data was developed at UC Berkeley with support from NSF grant AST-0071048.

REFERENCES

Anders, E., & Grevesse, N. 1989, Geochim. Cosmochim. Acta, 53, 197
Asplund, M., Grevesse, N., Sauval, A. J., & Scott, P. 2009, ARA&A, 47, 481
Barklem, P. S., & Aspelund-Johansson, J. 2005, A&A, 435, 373
Barklem, P. S., Piskunov, N., & O 'mara, B. J. 2000, Astron. Astrophys. Suppl. Ser, 142, 467
Bensby, T., Feltzing, S., & Oey, M. S. 2014, A&A, 562, A71
Brown, T. M., Smith, E., Ferguson, H. C., et al. 2006, ApJ, 652, 323
—. 2007, ApJL, 658, L95
—. 2009, ApJS, 184, 152
Carretta, E., Bragaglia, A., Gratton, R., D'Orazi, V., & Lucatello, S. 2009a, A&A, 508, 695
Carretta, E., Bragaglia, A., Gratton, R., & Lucatello, S. 2009b, A&A, 505, 139
Carretta, E., Bragaglia, A., Gratton, R., et al. 2010, ApJ, 712, L21
Castelli, F., Gratton, R. G., & Kurucz, R. L. 1997, Astron. Astrophys, 318, 841

Castelli, F., & Kurucz, R. L. 2004, ArXiv Astrophysics e-prints
Catelan, M., Borissova, J., Ferraro, F. R., et al. 2002, AJ, 124, 364
Cayrel, R., Depagne, E., Spite, M., et al. 2004, A&A, 416, 1117
Cenarro, A. J., Cardiel, N., Gorgas, J., et al. 2001, MNRAS, 326, 959
Chapman, S. C., Ibata, R., Lewis, G. F., et al. 2006, ApJ, 653, 255
Clementini, G., Contreras Ramos, R., Federici, L., et al. 2011, ApJ, 743, 19
Cohen, J. G., Huang, W., & Kirby, E. N. 2011, ApJ, 740, 60
Cohen, J. G., & Kirby, E. N. 2012, ApJ, 760, 86
Cohen, J. G., & Meléndez, J. 2005, AJ, 129, 303
Colucci, J. E., Bernstein, R. A., Cameron, S., McWilliam, A., & Cohen, J. G. 2009, ApJ, 704, 385
Cooper, A. P., Cole, S., Frenk, C. S., et al. 2010, MNRAS, 406, 744
Cooper, M. C., Newman, J. A., Davis, M., Finkbeiner, D. P., & Gerke, B. F. 2012, spec2d: DEEP2 DEIMOS Spectral Pipeline, Astrophysics Source Code Library
Cunningham, E. C., Deason, A. J., Guhathakurta, P., et al. 2016, ApJ, 820, 18
Demarque, P., Woo, J.-H., Kim, Y.-C., & Yi, S. K. 2004, ApJS, 155, 667
Faber, S. M., Phillips, A. C., Kibrick, R. I., et al. 2003, in SPIE, Vol. 4841, Instrument Design and Performance for Optical/Infrared Ground-based Telescopes, ed. M. Iye & A. F. M. Moorwood, 1657–1669
Font, A. S., Johnston, K. V., Ferguson, A. M. N., et al. 2008, ApJ, 673, 215
Fuhr, J. R., & Wiese, W. L. 2006, Journal of Physical and Chemical Reference Data, 35, 1669
Gilbert, K. M., Guhathakurta, P., Kalirai, J. S., et al. 2006, ApJ, 652, 1188
Gilbert, K. M., Fardal, M., Kalirai, J. S., et al. 2007, ApJ, 668, 245
Gilbert, K. M., Guhathakurta, P., Beaton, R. L., et al. 2012, ApJ, 760, 76
Gilbert, K. M., Kalirai, J. S., Guhathakurta, P., et al. 2014, ApJ, 796, 76
Gilmore, G., & Wyse, R. F. G. 1998, AJ, 116, 748
Girardi, L., Bertelli, G., Bressan, A., et al. 2002, A&A, 391, 195
Guhathakurta, P., Rich, R. M., Reitzel, D. B., et al. 2006, AJ, 131, 2497
Harris, W. E., Bell, R. A., Vandenberg, D. A., et al. 1997, AJ, 114, 1030
Hinkle, K., Wallace, L., Valenti, J., & Harmer, D. 2000, Visible and Near Infrared Atlas of the Arcturus Spectrum 3727-9300 A
Ho, N., Geha, M., Tollerud, E. J., et al. 2015, ApJ, 798, 77
Ibata, R., Irwin, M., Lewis, G., Ferguson, A. M. N., & Tanvir, N. 2001, Nature, 412, 49
Ibata, R. A., Lewis, G. F., McConnachie, A. W., et al. 2014, ApJ, 780, 128
Ishigaki, M. N., Chiba, M., & Aoki, W. 2012, ApJ, 753, 64
Johnston, K. V., Bullock, J. S., Sharma, S., et al. 2008, ApJ, 689, 936
Kacharov, N., Koch, A., & McWilliam, A. 2013, A&A, 554, A81
Kalirai, J. S., Gilbert, K. M., Guhathakurta, P., et al. 2006, ApJ, 648, 389
Kalirai, J. S., Zucker, D. B., Guhathakurta, P., et al. 2009, ApJ, 705, 1043
Kirby, E. N., & Cohen, J. G. 2012, AJ, 144, 168
Kirby, E. N., Cohen, J. G., Guhathakurta, P., et al. 2013, ApJ, 779, 102
Kirby, E. N., Cohen, J. G., Smith, G. H., et al. 2011a, ApJ, 727, 79
Kirby, E. N., Guhathakurta, P., Bolte, M., Sneden, C., & Geha, M. C. 2009, ApJ, 705, 328
Kirby, E. N., Guhathakurta, P., & Sneden, C. 2008a, ApJ, 682, 1217
Kirby, E. N., Guhathakurta, P., Zhang, A. J., et al. 2016, ApJ, 819, 135
Kirby, E. N., Lanfranchi, G. A., Simon, J. D., Cohen, J. G., & Guhathakurta, P. 2011b, ApJ, 727, 78
Kirby, E. N., Simon, J. D., Geha, M., Guhathakurta, P., & Frebel, A. 2008b, ApJ, 685, L43
Kirby, E. N., Guhathakurta, P., Simon, J. D., et al. 2010, ApJS, 191, 352
Koch, A., Rich, R. M., Reitzel, D. B., et al. 2008, ApJ, 689, 958
Kramida, A., Ralchenko, Y., Reader, J., & NIST ADS Team. 2016, NIST Atomic Spectra Database (version 5.4)
Kupka, F., Piskunov, N., Ryabchikova, T. A., Stempels, H. C., & Weiss, W. W. 1999, Astronomy and Astrophysics Supplement Series, 138, 119
Kurucz, R. L. 1992, Rev. Mexicana Astron. Astrofis., 23
—. 1993, Physica Scripta Volume T, 47, 110
Lanfranchi, G. A., & Matteucci, F. 2003, MNRAS, 345, 71
—. 2007, A&A, 468, 927
—. 2010, A&A, 512, A85
Lanfranchi, G. A., Matteucci, F., & Cescutti, G. 2006, A&A, 453, 67
Lianou, S., Grebel, E. K., & Koch, A. 2011, A&A, 531, A152
Newman, J. A., Cooper, M. C., Davis, M., et al. 2013, ApJS, 208, 5
Peterson, R. C., Dalle Ore, C. M., & Kurucz, R. L. 1993, ApJ, 404, 333
Ramírez, I., & Meléndez, J. 2005, ApJ, 626, 465
Richardson, J. C., Ferguson, A. M. N., Mackey, A. D., et al. 2009, MNRAS, 396, 1842
Shetrone, M., Venn, K. A., Tolstoy, E., et al. 2003, AJ, 125, 684
Shetrone, M. D., Côté, P., & Sargent, W. L. W. 2001, ApJ, 548, 592
Shetrone, M. D., Siegel, M. H., Cook, D. O., & Bosler, T. 2009, AJ, 137, 62
Simon, J. D., & Geha, M. 2007, ApJ, 670, 313
Sneden, C., Kraft, R. P., Prosser, C. F., & Langer, G. E. 1992, AJ, 104, 2121
Sneden, C., Pilachowski, C. A., & Kraft, R. P. 2000, AJ, 120, 1351
Sneden, C. A. 1973, PhD thesis, THE UNIVERSITY OF TEXAS AT AUSTIN.
Stanek, K. Z., & Garnavich, P. M. 1998, ApJ, 503, L131
Tanaka, M., Chiba, M., Komiyama, Y., et al. 2010, ApJ, 708, 1168
Tissera, P. B., White, S. D. M., & Scannapieco, C. 2012, MNRAS, 420, 255
Tollerud, E. J., Beaton, R. L., Geha, M. C., et al. 2012, ApJ, 752, 45
Tolstoy, E., Venn, K. A., Shetrone, M., et al. 2003, AJ, 125, 707
VandenBerg, D. A., Bergbusch, P. A., & Dowler, P. D. 2006, ApJS, 162, 375
Vargas, L. C., Geha, M. C., & Tollerud, E. J. 2014a, ApJ, 790, 73
Vargas, L. C., Gilbert, K. M., Geha, M., et al. 2014b, ApJ, 797, L2
Venn, K. A., Irwin, M., Shetrone, M. D., et al. 2004, AJ, 128, 1177
Weisz, D. R., Dolphin, A. E., Skillman, E. D., et al. 2014, ApJ, 789, 147

APPENDIX

MEAN METALLICITY: COMPARISON TO PREVIOUS WORK

In this work, we focus on the determination of [α/Fe] in M31 stellar halo RGB stars. Given the limited sample size of previously existing equivalent measurements, we can only directly compare our [α/Fe] measurements to the Vargas et al. (2014b) sample. However, an extensive body of literature exists on [Fe/H] estimates in the stellar halo of M31, which we discuss in detail here in the context of our measurements.

As presented in § 8.3, we find $\langle$[Fe/H]$\rangle$ = −1.53 dex and σ([Fe/H]) = 0.52 dex for f130_2. In contrast, Brown et al. (2007) estimated $\langle$[Fe/H]$\rangle_{\rm phot}$ = -0.87 dex for the nearby ACS field from color-magnitude diagram based SFHs, where their value is more metal-rich than our mean metallicity by 0.72 dex. In terms of both star counts and metallicity, Brown et al. (2007) characterized this field as straddling a transition region between the metal-rich inner halo and the metal-poor outer halo. Although the extended halo ($\gtrsim$ 60 kpc) is known to be metal-poor based on both photometric and Ca triplet metallicity indicators (Guhathakurta et al. 2006; Kalirai et al. 2006; Chapman et al. 2006; Koch et al. 2008; Gilbert et al. 2014; Ibata et al. 2014), a majority of photometric studies find that the inner halo (20–30 kpc) is as metal-rich as −0.7 dex for fields unpolluted by Giant Southern Stream debris (Guhathakurta et al. 2006; Gilbert et al. 2014). Based on an imaging survey, Ibata et al. (2014) found [Fe/H]$_{\rm phot}$ = −0.7 dex at 30 kpc for [α/Fe] = 0, where the mean metallicity does not decline to −1.5 dex until 150 kpc. Assuming [α/Fe] = 0.3 dex, Kalirai et al. (2006) found $\langle$[Fe/H]$\rangle_{\rm phot}$ = −1.48 dex and σ([Fe/H]$_{\rm phot}$) = 0.11 dex for the extended metal-poor halo ($\gtrsim$ 60 kpc). They based their measurements on photometry from fields with $\sim$1 hour DEIMOS spectroscopy, but they did not include f130_2 in their analysis of inner halo fields, for which they found $\langle$[Fe/H]$\rangle_{\rm phot}$ = −0.94 dex and σ([Fe/H]$_{\rm phot}$) = 0.60 dex around 30 kpc. Similarly, based on 397 stars between 20–40 kpc, Gilbert et al. (2014) found $\langle$[Fe/H]$\rangle_{\rm phot}$ = −0.70 dex and σ([Fe/H]$_{\rm phot}$) = 0.53 dex for [α/Fe] = 0 in this region (including more metal-rich Giant Southern Stream debris).

Clearly, our value of $\langle$[Fe/H]$\rangle$ = −1.53 dex for f130_2 is discrepant with photometric studies of M31's inner halo. This could be a consequence of selection effects against metal-rich stars, given that we discarded stars with strong TiO absorption (§ 8.2). However, we also consider alternative explanations. There are indications that (1) a smooth, metal-poor halo component with no detected substructure is found at all radii, and (2) the photometric metallicities likely overestimate the degree to which the inner halo is metal-rich. Using Ca triplet equivalent width measurements from stacked DEIMOS spectra, Chapman et al. (2006) analyzed major axis fields (and one minor axis field) in M31's stellar halo, finding evidence for a metal-poor stellar halo component ([Fe/H]$_{\rm CaT}$ = −1.4 dex) detectable at all radii between 10–70 kpc with no apparent metallicity gradient. In an analysis of M31's surface brightness profile, Gilbert et al. (2012) confirmed the detection of this distinct halo component. Additionally, Ibata et al.

(2014) found that the smooth halo is $\sim$0.2 dex more metal-poor than fields dominated by substructure, where metallicities of $-2.5 <$ [Fe/H] < -1.1 tend to characterize fields throughout the halo with little to no substructure. In contrast to Kalirai et al. (2006), Koch et al. (2008) analyzed the same DEIMOS fields (including f130_2) using Ca triplet metallicities, finding values systematically more metal-poor in mean metallicity by $\sim$0.75 dex. The large discrepancy likely results from differences in sample selection and metallicity measurement methodology (photometric vs. Ca triplet based).

Whether the methodology employed is photometric, Ca triplet based, or utilizes spectral synthesis can result in substantial differences in metallicity estimates for the same sample (e.g., Lianou et al. 2011). Most relevantly, photometric studies often assume [α/Fe] = 0, which can inflate metallicity estimates significantly compared to assuming an α-enhanced field. Using VandenBerg et al. (2006) isochrones, assuming 10 Gyr old stellar populations (Brown et al. 2007), a distance modulus of $(m-M)_0$ = 24.63 $\pm$ 0.20 (Clementini et al. 2011), and [α/Fe] = 0 dex, we found $\langle$[Fe/H]$\rangle_{\rm phot} = -1.40$ dex for our sample of 14 M31 RGB stars. If we instead assume [α/Fe] = 0.3, we obtain $\langle$[Fe/H]$\rangle_{\rm phot} = -1.59$ dex, corresponding to a decrease in the mean photometric metallicity of 0.19 dex. We find nearly identical results by repeating the calculation with a different set of isochrones (Demarque et al. 2004).

The assumptions intrinsic to photometric metallicities, combined with the large amount of tidal debris present in the inner halo of M31 that is included in many previously published measurements in this radial range, are sufficient to explain the large difference between our value of $\langle$[Fe/H]$\rangle$ for f130_2 and previous analyses in the inner halo of M31. A primary strength of our study is that we can determine both [α/Fe] and [Fe/H] from spectroscopy, without prior assumptions on either parameter. We acknowledge that we may be preferentially sampling brighter, more metal-poor stars in this field, given that we are S/N-limited and select against stars with strong TiO absorption. However, given that we can measure both [Fe/H] and [α/Fe] reliably from some of the highest quality spectra in M31's halo yet obtained, we conclude that $\langle$[Fe/H]$\rangle = -1.53$ dex is likely an accurate representation of our final sample's mean metallicity. Thus, it is possible that our sample in f130_2 represents the metal-poor halo that underlies substructure (Chapman et al. 2006; Gilbert et al. 2014; Ibata et al. 2014) in the inner halo of M31.